Estimation of Gravity Wave Momentum Flux and Phase Speeds from Quasi-Lagrangian Stratospheric Balloon Flights. Part I: Theory and Simulations

GILLIAN BOCCARA AND ALBERT HERTZOG

Laboratoire de Météorologie Dynamique, Université Pierre et Marie Curie, École Polytechnique, Palaiseau, France

ROBERT A. VINCENT

Department of Physics, University of Adelaide, Adelaide, Australia

FRANÇOIS VIAL

Laboratoire de Météorologie Dynamique, École Polytechnique, Palaiseau, France

(Manuscript received 11 December 2007, in final form 17 March 2008)

ABSTRACT

A methodology for estimating gravity wave characteristics from quasi-Lagrangian observations provided by long-duration, superpressure balloon flights in the stratosphere is reviewed. Wavelet analysis techniques are used to detect gravity wave packets in observations of pressure, temperature, and horizontal velocity. An emphasis is put on the estimation of gravity wave momentum fluxes and intrinsic phase speeds, which are generally poorly known on global scales in the atmosphere. The methodology is validated using Monte Carlo simulations of time series that mimic the balloon measurements, including the uncertainties associated with each of the meteorological parameters. While the azimuths of the wave propagation direction are accurately retrieved, the momentum fluxes are generally slightly underestimated, especially when wave packets overlap in the time–frequency domain, or for short-period waves. A proxy is derived to estimate by how much momentum fluxes are reduced by the analysis. Retrievals of intrinsic phase speeds are less accurate, especially for low phase speed waves. A companion paper (Part II) implements the methodology to observations gathered during the Vorcore campaign that took place in Antarctica between September 2005 and February 2006.

1. Introduction

Temperatures in the extratropical middle atmosphere differ greatly from radiative equilibrium values (Andrews et al. 1987). The observed departures result from a global pole-to-pole circulation in the middle atmosphere driven by planetary and gravity wave breaking in the stratosphere and mesosphere (Holton et al. 1995). Because of their shorter spatial and temporal scales, as well as their small amplitudes in the lower atmosphere, gravity waves (GWs) are more difficult to observe than planetary waves. In particular, there are relatively few observations of the global-scale distribution of GWs available, despite their importance in the dynamics of the middle atmosphere (e.g., Nastrom and Fritts 1992; Fritts and Nastrom 1992; Allen and Vincent 1995). In the past few years, however, modern spaceborne observations have significantly improved our knowledge of the GW field in the middle atmosphere. For example, limb observations of infrared (Fetzer and Gille 1994; Eckermann and Preusse 1999; Preusse et al. 2002) and microwave radiances (Wu and Waters 1996; McLandress et al. 2000; Jiang et al. 2004), nadir observations (Wu 2004; Eckermann and Wu 2006; Alexander and Barnet 2007), as well as GPS radio-occultation techniques (Steiner and Kirchengast 2000; Tsuda et al. 2000; Ratnam et al. 2004; Baumgaertner and McDonald 2007), provide important insights into the distribution of GW potential energy on a global scale.

Nevertheless, a GW quantity that is still poorly measured on a global scale is the momentum flux, although

Corresponding author address: Albert Hertzog, Laboratoire de Météorologie Dynamique, École Polytechnique, F-91128 Palaiseau CEDEX, France.
E-mail: albert.hertzog@lmd.polytechnique.fr

DOI: 10.1175/2008JAS2709.1

it is a quantity required to constrain GW effects in atmospheric general circulation models (Charron et al. 2002; McLandress and Scinocca 2005). Some GW momentum fluxes measurements have been obtained at a few widely spaced locations around the globe with radar or in situ airborne observations (e.g., Vincent and Reid 1983; Tsuda et al. 1990; Fritts et al. 1990; Alexander and Pfister 1995). Recently, the first global observations of absolute GW momentum fluxes in the lower stratosphere were obtained during two one-week duration campaigns using the Cryogenic Infrared Spectrometers and Telescopes for the Atmosphere (CRISTA) instrument (Ern et al. 2004, 2006). Furthermore, Alexander et al. (2008) derived absolute momentum fluxes from the High Resolution Dynamics Limb Sounder (HIRDLS) observations in May 2006. Long-duration flights of superpressure balloons in the lower stratosphere provide an additional method by which GW momentum fluxes can be derived on global scales (Massman 1981; Hertzog and Vial 2001; Vincent et al. 2007). The balloon technique complements satellite observations by providing an independent estimation of absolute GW momentum fluxes. Importantly, directional fluxes, which cannot be measured using current spaceborne technology, can be derived with the balloon technique.

Here we review and extend the methodology used to extract GW information from observations obtained during long-duration balloon flights. In contrast to Hertzog and Vial (2001), we take into account that superpressure balloons do not perfectly follow constant-density (isopycnic) surfaces and assess this effect in the retrieval of GW momentum fluxes. Furthermore, we derive an expression for computing GW phase speeds from the balloon observations. Last, we carefully quantify the accuracy with which GW characteristics are retrieved from such datasets. In a companion paper (Hertzog et al. 2008), the methodology described in this study is applied to the dataset collected during the 2005 Stratéole/Vorcore campaign, during which 27 superpressure balloons were launched from McMurdo, Antarctica (77.8°S, 166.7°E) (Hertzog et al. 2007). During the campaign, the scientific payload carried by each balloon recorded every 15 min the air temperature and pressure, as well as the balloon's 3D position. Since superpressure balloons are very good tracers of horizontal motions in the atmosphere (Massman 1978), the horizontal positions provide information on the horizontal wind velocities during the flights. The methodology described in this study can, in principle, be used with any quasi-Lagrangian balloon flight. However, the reported uncertainties in the derived GW properties are specifically valid for the Vorcore observations since they depend on, among other things, the observational noise and sampling rate.

The following section reviews the theoretical basis behind the retrieval of GW characteristics from long-duration balloon observations. The important point of such observations is that the balloons move with the wind so that the GW disturbances observed by the balloons are made in a Lagrangian frame of reference. The method used to estimate momentum fluxes, as well as wave phase speeds, from those observations is presented. Section 3 describes the numerical simulations undertaken to estimate the accuracy of our GW retrievals. Specifically, we generated time series containing a number of GW packets with known characteristics, similar to those recorded during real balloon flights. The algorithm used to analyze these simulated time series or the real ones is also described in this section. Section 4 is devoted to comparisons of the retrieved GW characteristics with those imposed in the simulated time series. We consider in particular the retrieval of absolute as well as zonal and meridional momentum fluxes and phase speeds as these parameters are arguably the most important in GW drag parameterizations. The limits of the GW retrievals are also discussed. The main results of this study are summarized in the final section.

2. Theory

Here, the relationships between the various meteorological parameters measured by superpressure balloons (SPBs) when they encounter gravity wave packets are examined. Based on these equations, the methodology used to infer GW properties is developed in two steps: first, we consider that SPBs drift on constant-density (isopycnic) surfaces (Massman 1978), and then take into account the effect of small departures from a perfect isopycnic behavior, as suggested in Nastrom (1980). In particular, Nastrom showed that the balloon vertical displacements may have a small phase shift relative to those of an isopycnic surface. In both cases, we assume that SPBs are perfect tracers of the horizontal wind (Hertzog et al. 2007).

a. The balloon as a perfect isopycnic tracer

Figure 1 illustrates (in solid) the vertical displacement of an isopycnic surface induced by a gravity wave. We assume here that the balloon always remains on this surface. Let A (altitude z_0) be a point where the wave-induced density disturbance vanishes. At A, the density therefore simply reduces to the background atmospheric density $\bar{\rho}(z_0)$. Let B be a point where the ver-

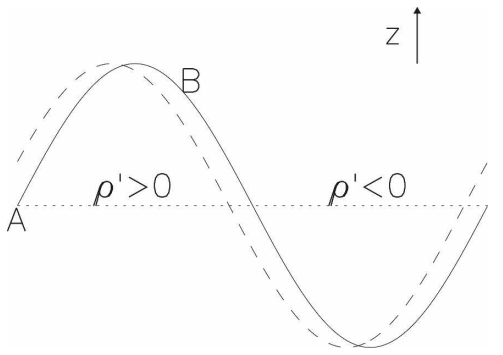

FIG. 1. Vertical displacements of an isopycnic surface generated by an Eulerian disturbance in air density ρ' induced by a gravity wave (solid line). In A, $\rho' = 0$, whereas in B, $\rho' \neq 0$ (see text for further details). A perfect isopycnic balloon will drift on the isopycnic surface, whereas according to Massman (1978) the vertical displacement of real balloons (dashed) may be slightly shifted relative to the isopycnic surface.

tical displacement ζ'_ρ of the isopycnic surface is nonzero, where the prime denotes a wave disturbance. The density at B is

$$\rho(z_0 + \zeta'_\rho) = \overline{\rho}(z_0 + \zeta'_\rho) + \rho'(z_0 + \zeta'_\rho). \tag{1}$$

By definition, it is equal to the density at A so that at first order of the wave disturbance:

$$\overline{\rho}(z_0) = \overline{\rho}(z_0) + \frac{\partial \overline{\rho}}{\partial z}\zeta'_\rho + \rho'(z_0). \tag{2}$$

Solving for the vertical displacement of the isopycnic surface yields

$$\zeta'_\rho = -\frac{\rho'(z_0)}{\partial \overline{\rho}/\partial z} = H\frac{\rho'(z_0)}{\overline{\rho}(z_0)}, \tag{3}$$

where

$$H \equiv -\frac{1}{\overline{\rho}}\frac{\partial \overline{\rho}}{\partial z}$$

is the density scale height.

The wave-induced pressure perturbation in B is obtained as in (1):

$$p(z_0 + \zeta'_\rho) = \overline{p}(z_0) + \zeta'_\rho\frac{\partial \overline{p}}{\partial z} + p'(z_0). \tag{4}$$

Hence the pressure perturbation observed by the balloon (i.e., the Lagrangian pressure perturbation) at B is, to first order,

$$p'_l(B) = p(z_0 + \zeta'_\rho) - \overline{p}(z_0) = p'(z_0) + \zeta'_\rho\frac{\partial \overline{p}}{\partial z}, \tag{5}$$

where the index l denotes Lagrangian disturbances. It should be noted that the second-order Stokes correction to the Lagrangian-mean pressure has been neglected in this equation. The Lagrangian pressure perturbations measured by the drifting balloon are therefore the sum of two components: (i) the Eulerian perturbation caused by the wave $p'(z_0)$, hereafter referred to as p'_w, and (ii) a contribution associated with the vertical gradient of the background pressure $\zeta'_\rho\partial\overline{p}/\partial z$, hereafter referred to as p'_g. Similar equations can be written for the velocity perturbations, but we assume in the following that $u'_g = \zeta'_\rho\partial\overline{u}/\partial z$ and $v'_g = \zeta'_\rho\partial\overline{v}/\partial z$ are small with respect to the Eulerian perturbations (see, e.g., Hertzog and Vial 2001).

From now on, a complex notation is used for the wave disturbances with primed quantities denoting the complex wave amplitudes. The following developments rely on the classical GW equations derived in Fritts and Alexander (2003). Thus, the horizontal momentum equations can be used to find a relation between the Eulerian pressure disturbance and the velocity perturbation in the direction of propagation of the wave $u'_\parallel$:

$$p'_w = \overline{\rho}\hat{c}\delta_- u'_\parallel, \tag{6}$$

where $\delta_- = 1 - f^2/\hat{\omega}^2$ (with f the inertial frequency and $\hat{\omega}$ the intrinsic frequency of the wave) and $\hat{c}$ is the horizontal intrinsic phase speed of the wave (i.e., $\hat{c} = \hat{\omega}/k_h$, where k_h is the horizontal wavenumber). The vertical momentum equation [Eq. (17) in Fritts and Alexander (2003)], on the other hand, relates the Eulerian pressure and density perturbations:

$$-i\hat{\omega}w' + \left(im - \frac{1}{2H}\right)\frac{p'_w}{\overline{\rho}} = -g\frac{\rho'}{\overline{\rho}}, \tag{7}$$

where w' is the vertical velocity perturbation, and m is the vertical wavenumber. Owing to the sampling period of 15 min used during Vorcore, we cannot resolve the highest frequency part of the gravity wave spectrum. The motions that we are interested in are therefore to a good approximation hydrostatic, and we can safely ignore the first term on the left-hand side of (7).

Assuming that the background pressure is in hydrostatic equilibrium, p'_g can be expressed as

$$p'_g = -\overline{\rho}g\zeta'_\rho. \tag{8}$$

Combining (3) with (7) and (8), p'_g can be expressed in terms of p'_w, so the Lagrangian pressure perturbation becomes

$$p'_l = \left(\frac{1}{2} + imH\right)p'_w. \tag{9}$$

Using (6) the Lagrangian pressure perturbation can then be related to the velocity perturbation in the wave direction of propagation:

$$p'_l = \left(\frac{1}{2} + imH\right)\overline{\rho}\hat{c}\delta_- u'_{\|}. \tag{10}$$

It is interesting to note that for a typical GW vertical wavelength of 3 km in the polar lower stratosphere (Allen and Vincent 1995) (i. e., $m \sim 2 \times 10^{-3}$ rad m^{-1}) and with $H \sim 6$ km, the imaginary part of (10), which is associated with p'_g, dominates the real part so that p'_l and $u'_{\|}$ are essentially in quadrature, whereas the Eulerian pressure disturbance is in phase with $u'_{\|}$.

Forming the covariance of p'_l with $u'_{\|}$, one obtains

$$p'_l u'^*_{\|} = \frac{\overline{\rho}\hat{c}\delta_-}{2} u'^2_{\|} + imH\overline{\rho}\hat{c}\delta_- u'^2_{\|}, \tag{11}$$

where the asterisk denotes the complex conjugate. The horizontal intrinsic phase speed of the wave can thus be computed from this covariance:

$$\hat{c} = \frac{2}{\overline{\rho}\delta_- u'^2_{\|}} \Re(p'_l u'^*_{\|}), \tag{12}$$

where $\Re$ stands for the real part.

To obtain an expression for the wave absolute momentum flux, we first use the polarization relation between w' and $u'_{\|}$ (Fritts and Alexander 2003):

$$w' = \left(-\frac{i}{2H} - m\right)\frac{\hat{\omega}^2 - f^2}{k_h N^2} u'_{\|}, \tag{13}$$

where N is the buoyancy frequency. Using (11)

$$\Re(w' u'^*_{\|}) = -\frac{\hat{\omega}}{\overline{\rho}HN^2} \Im(p'_l u'^*_{\|}), \tag{14}$$

where $\Im$ stands for the imaginary part. Note that we are only interested in the real part of the momentum flux as it is the only contribution that does not vanish when averaged over a wave period.

Simple calculus shows that the multiplicative term on the right-hand side in the previous equation depends on the vertical gradient of background temperature, so

$$\frac{1}{\overline{\rho}HN^2} = \frac{1}{\overline{\rho}g}\frac{g/R + \partial\overline{T}/\partial z}{g/c_p + \partial\overline{T}/\partial z}, \tag{15}$$

where R and c_p are, respectively, the perfect gas constant and specific heat at constant pressure per unit mass of air. Equations (14) and (15) are equivalent to (11) in Hertzog and Vial (2001).

b. Real balloon

In high static stability conditions, such as those encountered in the stratosphere, superpressure balloons behave asymptotically as isopycnic tracers (Massman 1978). Nevertheless, Nastrom (1980) showed that the vertical displacement of a balloon (ζ'_b) can slightly lead that of the isopycnic surface. We now study the effect of this small shift. Let ϕ (>0) be the small angle by which the balloon leads the isopycnic surface (see also Fig. 1):

$$\zeta'_b = \zeta'_\rho e^{-i\phi} \approx \zeta'_\rho(1 - i\phi). \tag{16}$$

The expression for p'_g is modified accordingly:

$$p'_g = -\overline{\rho}g\zeta'_\rho(1 - i\phi), \tag{17}$$

while p'_w is unchanged to first order. The resulting new expression for the Lagrangian pressure perturbation becomes

$$p'_l = \left[\left(\frac{1}{2} + mH\phi\right) + i\left(mH + \frac{\phi}{2}\right)\right]\overline{\rho}\hat{c}\delta_- u'_{\|}. \tag{18}$$

Now $mH \gg \phi/2$ for typical values of m and H so that, when forming the covariance with $u'_{\|}$,

$$p'_l u'^*_{\|} \approx \left(\frac{1}{2} + mH\phi\right)\overline{\rho}\hat{c}\delta_- u'^2_{\|} + imH\overline{\rho}\hat{c}\delta_- u'^2_{\|}. \tag{19}$$

Hence the imaginary part is not modified by the phase shift ϕ, and the wave momentum flux can still be estimated using (14). On the other hand, estimation of the wave intrinsic phase speed now requires knowledge of ϕ. To estimate ϕ from the balloon data, we consider the density recorded by the balloon; namely,

$$\rho_b(z) = \overline{\rho}(z) + \frac{\partial\overline{\rho}}{\partial z}\zeta'_b + \rho'(z). \tag{20}$$

Using (3) and (16) gives

$$\rho_b(z) = \overline{\rho}(z) + (1 - i\phi)\left\{H\frac{\rho'(z)}{\overline{\rho}(z)}\left[-\frac{\overline{\rho}(z)}{H}\right]\right\} + \rho'(z) \tag{21}$$

$$= \overline{\rho}(z) + i\phi\rho'(z) \tag{22}$$

to first order. Hence, the Lagrangian density perturbation is

$$\rho'_l = \rho_b - \overline{\rho} = i\phi\rho'. \tag{23}$$

Using (6) and (7) gives

$$\rho'_l = \left(m + \frac{i}{2H}\right)\phi\frac{\overline{\rho}\hat{c}\delta_-}{g} u'_{\|}. \tag{24}$$

Forming the covariance of ρ'_l with $u'_{\|}$ and taking the real part yields

$$\Re(\rho'_l u'^*_{\|}) = m\phi\frac{\overline{\rho}\hat{c}\delta_-}{g} u'^2_{\|}; \tag{25}$$

hence, ϕ can be determined via

$$\phi = gH \frac{\Re(\rho_i' u_\parallel'^*)}{\Im(p_i' u_\parallel'^*)}. \quad (26)$$

Once ϕ is estimated, the velocity perturbation can be computationally shifted to retrieve the intrinsic phase speed of the wave:

$$\hat{c} = \frac{2}{\overline{\rho}\delta_- u_\parallel'^2} \Re[p_i'(u_\parallel' e^{-i\Phi})^*]. \quad (27)$$

The algorithm used to analyze the long-duration balloon dataset therefore uses (14) and (27) to estimate both the momentum flux and the intrinsic phase speed of the observed GW packets. It ultimately relies on the estimation of phase differences between the observed velocity and pressure time series.

3. Simulations and the retrieval algorithm

In this section, we discuss numerical simulations that were conducted to assess the validity of our retrievals of GW characteristics from the SPB dataset. We then present in more detail the algorithm used to analyze the observations.

a. Numerical simulations of balloon observations

A three-dimensional model was constructed to simulate the balloon observations. It consists of a background isothermal atmosphere, with a constant buoyancy frequency ($N = 2.1 \times 10^{-2}$ rad s^{-1}) and a mean eastward flow of 10 m s^{-1} that is representative of conditions during Vorcore. One or several gravity wave packets, each propagating upward in the atmosphere, were linearly superimposed onto this background. GW polarization relations (Andrews et al. 1987; Fritts and Alexander 2003) were used to compute the wave-induced disturbances in horizontal velocity, pressure, temperature, and density. Wave–wave and wave–mean flow interactions were ignored. GW characteristics, such as the phase constant ψ, intrinsic period $2\pi/\hat{\omega}$, azimuth of propagation θ, intrinsic phase speed $\hat{c}$, and time corresponding to the center of the wave packet t_c, were chosen randomly within the ranges detailed in Table 1. The wave packets had a Gaussian envelope, with full width at half maximum (FWHM) proportional to the intrinsic period of the wave so that the wave packets always had the same number of oscillations (~3). Finally, a phase shift (ϕ) between the balloon vertical displacement and that of the isopycnic surface was randomly chosen from a homogeneous distribution between 0 and 0.5 rad and assigned to each wave packet so as to simulate the departure of the balloon from isopycnicity. From the randomly chosen parameters the horizontal and vertical wavenumbers were derived as

TABLE 1. Gravity wave characteristics used in the simulations. The longest period used corresponds to the inertial period at 60° latitude.

Parameter	Range
Phase at origin (ψ)	0–2π
Horizontal angle of propagation (θ)	0–2π
Intrinsic period ($2\pi/\hat{\omega}$)	1–13.9 h
Intrinsic phase speed ($\hat{c}$)	0–120 m s^{-1}
Time of occurrence (t_c)	0.5–9.5 day
Envelope type	Gaussian
FWHM of the envelope	$1.7 \times 2\pi/\hat{\omega}$
Phase shift of balloon response (ϕ)	0–0.5 (rad)

$$k_h = \frac{\hat{\omega}}{\hat{c}} \quad (28)$$

and

$$m = -\sqrt{\frac{N^2 - \hat{\omega}^2}{\hat{\omega}^2 - f^2} k_h^2 - \frac{1}{4H^2}}. \quad (29)$$

The negative value of the vertical wavenumber means that the waves were propagating upward.

The amplitudes of the wave-induced disturbances in horizontal velocity along the directions of propagation were chosen so as to be consistent with the horizontal kinetic-energy density spectrum displayed in Hertzog and Vial (2001) and Hertzog et al. (2002). In particular, the wave amplitude scales as $\hat{\omega}^{-1}$ in our simulations. The vertical momentum flux transported by the wave packets is computed analytically from the wave parameters and the Gaussian envelope.

For some simulations, the combination of parameters generated unstable waves. In the real atmosphere, such wave-generated instabilities will significantly reduce the wave amplitudes. Simulations that included unstable waves were therefore discarded. To determine whether a wave packet would be unstable, we used a similar threshold to that advocated by Fritts et al. (2006); namely,

$$\frac{\zeta'}{\lambda_z} < 0.1, \quad (30)$$

where ζ' is the amplitude of the wave-induced vertical displacements of air parcels and λ_z is the vertical wavelength. Simulations that contained quasi-inertial wave packets ($\hat{\omega} < 1.1f$) or wave disturbances that occurred too close to the beginning or end of the simulated flights (i.e., those for which less than two periods could be observed in the simulated time series) were also removed from further analysis.

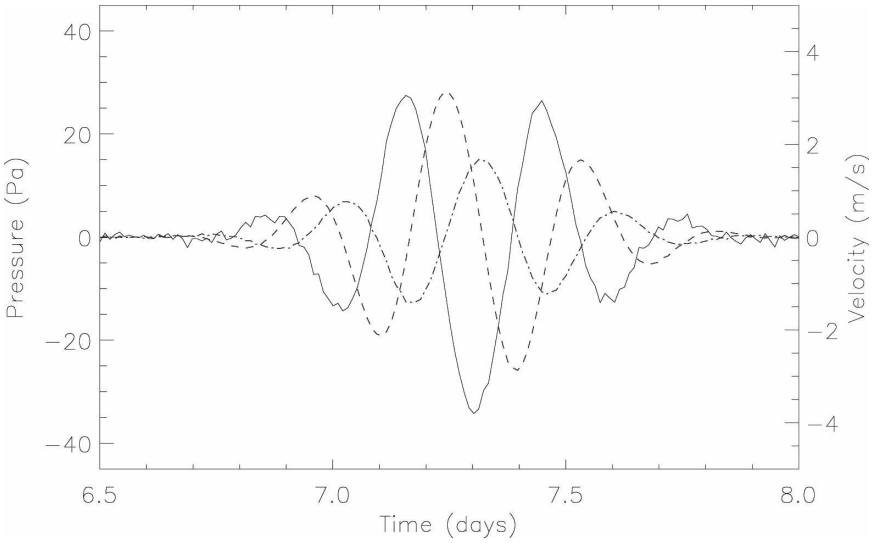

FIG. 2. Simulated gravity wave disturbances in pressure (solid, left scale) and in zonal (dashed, right scale) and meridional (dashed–dotted, right scale) velocities. Measurement noise is included in the simulated time series and is particularly evident in the pressure disturbance.

The simulated flights had a duration of 10 days and started from 60°S. The simulated observations mimic those of the real balloons. In particular, the same 15-min sampling rate was used, and the horizontal velocities were computed through finite differences of successive balloon positions. The simulations were run with and without an additional Gaussian white noise to assess the importance of measurement uncertainties in the analysis. The standard deviations of the added noise correspond to the accuracy of the sensors used on real balloons—0.25 K for temperature, 1 Pa for pressure and 15 m for the horizontal position provided by absolute GPS measurements. An example of simulated gravity wave disturbances is displayed in Fig. 2. This figure highlights the relatively greater importance of the measurement uncertainties in the pressure records compared to those associated with horizontal velocities. It is also noticeable that the zonal velocity fluctuations lead those in the meridional component, consistent with the fact that the balloons are drifting in the Southern Hemisphere.

b. Retrieval algorithm

In the balloon observations, GWs often appear as individual wave packets. Wavelet analysis techniques were therefore chosen to retrieve GW characteristics since they enable us to account for the nonstationarity of the wave field. Applied to either real or simulated SPB time series, the wavelet technique provides information in time–(intrinsic) frequency space. The algorithm uses a complex Morlet wavelet as the retrieval of wave momentum fluxes and phase speeds is based on phase differences between the various time series. The main steps of the retrieval algorithm are as follows:

1. The time series of pressure, horizontal velocity, temperature, and density are decomposed using wavelet techniques. Morlet wavelets with periods ranging between 1 and 24 h are used. This analysis provides complex coefficients that are representative of the energy and phase of the decomposed signal in small time/(intrinsic) frequency bins. The wavelet coefficients are normalized so that the variance of each decomposed signal is recovered when summed over the whole of the modulus of the squared coefficients (Torrence and Compo 1998). From now on, tildes are used to denote wavelet coefficients. For example, $\tilde{p}(t_i, \hat{\omega}_j)$ corresponds to the decomposed pressure time series on the jth wavelet, whose central frequency is $\hat{\omega}_j$, in the neighborhood of the ith observation point.
2. To avoid interpreting noise as GWs, wavelet coefficients for which the modulus is smaller than three times the standard deviation of the observational uncertainties are discarded.
3. To determine the horizontal direction of propagation to within an ambiguity of 180°, the horizontal velocity coefficients $\tilde{u}(t_i, \hat{\omega}_j)$ and $\tilde{v}(t_i, \hat{\omega}_j)$ are rotated until the velocity parallel to the rotated direction is maximized. Let $\tilde{u}_{\parallel}$ and $\tilde{u}_{\perp}$ be the respective velocity wavelet coefficients in the parallel and perpen-

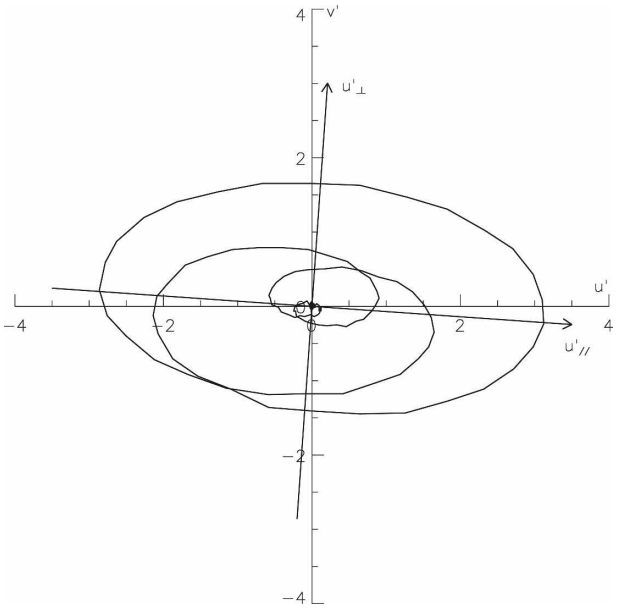

FIG. 3. Hodograph of the horizontal velocity fluctuations associated with the GW packet shown in Fig. 2. Units are in m s^{-1}. The wave direction of propagation (356° from east) is indicated by the arrow pointing to $u'_{\|}$. The horizontal velocities projected on this direction and on the orthogonal direction are referred to as $u'_{\|}$ and $u'_{\perp}$, respectively, in the text.

dicular directions. The 180° ambiguity is resolved by assuming that wave packets propagate upward in the atmosphere, so the absolute momentum flux $\Re(\tilde{u}_{\|} w^*)$ obtained from (14) is necessarily positive. Figure 3 illustrates this detection for the wave packet shown in Fig. 2. In this case, the input and retrieved direction of propagation are 356° from east.

4. Each wave packet actually projects onto several wavelets, so the central frequency of a wave packet must be known in order to retrieve the momentum flux [see Eq. (14)]. This is achieved by using the polarization relation that links the parallel to the perpendicular velocity disturbances (Fritts and Alexander 2003). Specifically, the wavelet coefficients that satisfy

$$\tilde{u}_{\|}(t_i, \hat{\omega}_j) = -i \frac{\hat{\omega}_j}{f_i} \tilde{u}_{\perp}(t_i, \hat{\omega}_j) \tag{31}$$

to within an assumed uncertainty (typically 50%) are selected as being associated with the wave packet centers. In (31), f_i is the inertial frequency corresponding to the balloon latitude at time t_i. This search is only performed among those frequencies that satisfy $\hat{\omega}_j > f_i$, that is, those corresponding to gravity waves. Note that this algorithm can, in principle, detect several wave packet centers at the same observation time. We use $[\hat{\omega}^c_k(t_i)]_k$ to denote the set of wavelet frequencies corresponding to these central coefficients.

5. Next, the envelopes of the wave packets are identified. This is done by searching in the frequency space around each $\hat{\omega}^c_k(t_i)$ and selecting the neighboring frequencies for which

$$\Re[\tilde{u}_{\|}\tilde{w}^*(t_i, \hat{\omega}_j)] \geq \frac{\Re\{\tilde{u}_{\|}\tilde{w}^*[t_i, \hat{\omega}^c_k(t_i)]\}}{10}. \tag{32}$$

In contrast with the previous step, this latter search is not limited to GW frequencies alone, as the wave packet may project on wavelets with frequencies smaller than the local inertial frequency. The wavelet frequencies selected during this step are those associated with a gravity wave packet, hereafter referred to as $\hat{\omega}^{\mathrm{gw}}(t_i)$. Figure 4 demonstrates the two last steps for the time series corresponding to the wave packet shown in Fig. 2. The estimated wave envelope is displayed in the left panel in the time–frequency plane, whereas the right panel shows the selected frequencies at one specific time. In this case, with only one wave packet in the simulation, the algorithm obviously succeeds in identifying the wave envelope. Some arguably false detections at periods much longer than the wave central period are nevertheless observed. They are, however, of little significance for the GW retrievals since the momentum fluxes associated with these wavelet coefficients are very small.

6. The contribution of the absolute GW momentum flux at time t_i to the flight-mean absolute momentum flux is computed by summing over the selected frequencies; that is,

$$\sum_j \Re\{\tilde{u}_{\|}\tilde{w}^*[t_i, \hat{\omega}^{\mathrm{gw}}_j(t_i)]\}. \tag{33}$$

The phase speeds, on the other hand, are estimated for each of the wave packets present at time t_i. Equation (27) is used at the central frequency $\hat{\omega}^c_k(t_i)$ to compute the phase speed of each wave packet. This phase speed is then assigned to the frequencies representative of the wave packet envelope.

4. Results

Monte Carlo simulations were performed to assess statistically the accuracy of the algorithm used to retrieve GW characteristics. We first present the results obtained with a single gravity wave in the simulated time series and then consider the more realistic situation in which several wave packets are present and may overlap in time–frequency space. Unless otherwise

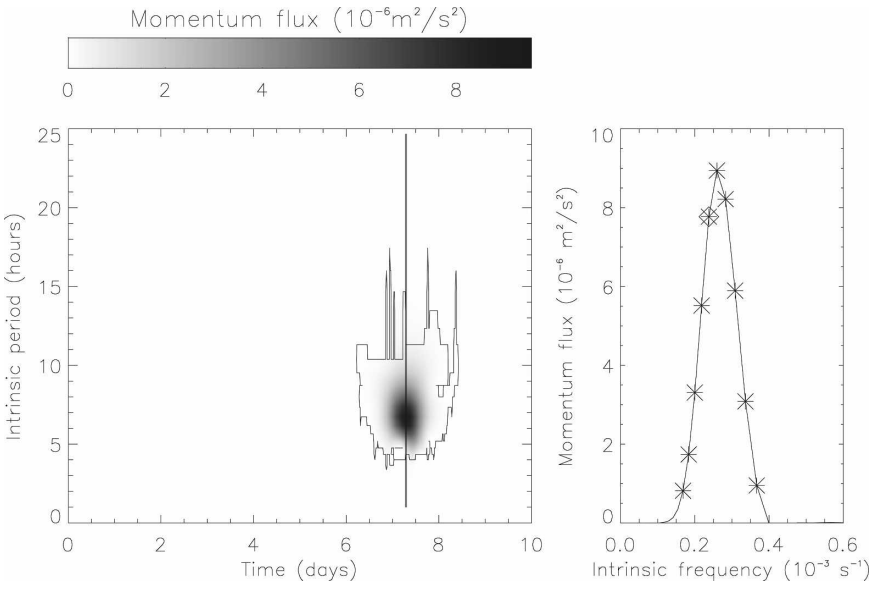

FIG. 4. (left) Momentum-flux distribution in time/intrinsic-period space for the time series shown in Fig. 2. The area enclosed by the solid line corresponds to the detected envelope of the wave packet (see text). (right) Cross section of momentum flux vs intrinsic frequency at the time indicated by the solid line in the left panel. The diamond shows the detected central frequency of the wave packet. The frequencies associated with the wave packet are indicated by star symbols.

stated, the results presented below refer to simulations that include measurement uncertainties.

a. Simulations with one gravity wave packet

One thousand time series simulating balloon flights disturbed by one GW packet were numerically generated and analyzed with the algorithms described in the previous section. For each simulation the flight-mean GW momentum flux was retrieved and directly compared to the flight-mean "true" momentum flux computed from the input wave packet parameters. To estimate the accuracy with which the phase speeds and directions of propagation are retrieved, a flight-mean intrinsic phase speed and direction of propagation were also computed through a momentum-flux weighted average over the selected wavelet coefficients. For instance, the retrieved flight-mean intrinsic phase speed is obtained as

$$\bar{\hat{c}} = \frac{\sum_i \sum_j \hat{c}[t_i, \hat{\omega}_j^{\mathrm{gw}}(t_i)]\, \Re\{\tilde{u}_\parallel \tilde{w}^*[t_i, \hat{\omega}_j^{\mathrm{gw}}(t_i)]\}}{\sum_i \sum_j \Re\{\tilde{u}_\parallel \tilde{\omega}^*[t_i, \hat{\omega}_j^{\mathrm{gw}}(t_i)]\}}, \quad (34)$$

where the inner sums extend over the frequencies associated with a wave packet at time t_i.

Figure 5 shows the retrieved propagation directions with respect to the input values. Clearly, the retrievals do not exhibit any significant bias. On the basis of these Monte Carlo simulations, the standard deviation of the retrievals is 2°. The wave propagation directions are well estimated as they rely only on the velocity observations, which have small uncertainties relative to the amplitude of the wave-induced velocity disturbances, whatever the intrinsic frequencies of the wave packets.

Figure 6 displays the performance of the analysis in retrieving the flight-mean absolute momentum fluxes. In general, the algorithm succeeds in estimating the momentum fluxes, although a slight systematic underestimation is observed. This underestimation results from the way in which the algorithm selects the wavelet coefficients. Overall, in this case with one gravity wave

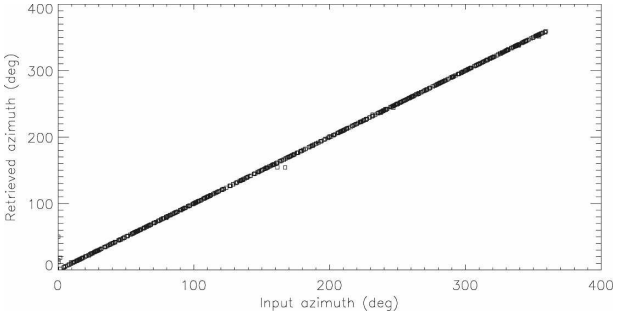

FIG. 5. Retrieved vs input horizontal direction of propagation of wave packets for simulated flights with one gravity wave.

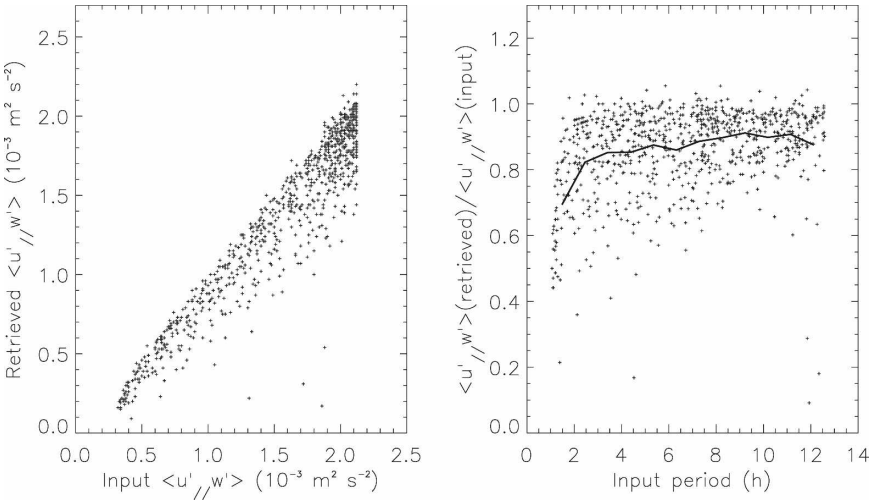

FIG. 6. (left) As in Fig. 5 but for the flight-mean absolute momentum flux. (right) Ratio of retrieved to input flight-mean absolute momentum flux vs intrinsic period of the wave packets. The thick line indicates the mean ratio over period intervals of 1 h.

packet in each simulation, the mean and standard deviation of the ratios between the retrieved momentum flux values and the input values are, respectively, 0.86 and 0.13; that is, the momentum fluxes are underestimated by 14% ± 13% (1σ). The right panel of Fig. 6 shows the ratio of the retrieved to the input momentum fluxes versus the intrinsic periods of the wave packets. It is noticeable that the momentum flux underestimation occurs mostly at intrinsic periods of a few hours, as well as at periods very close to the inertial frequency. For small periods, the discrepancy results mainly from the finite sampling rate of the balloon observations. As previously mentioned, the retrieval algorithm is based on the estimation of phase differences between time series, which incurs significant inaccuracy when the sampling rate is comparable to the wave period. At quasi-inertial periods, on the other hand, the underestimation results from the small vertical displacements for these wave packets. In this case, the pressure-induced perturbations (i.e., p'_g) become comparable to the uncertainty in the pressure measurements, causing a deterioration in the momentum flux retrieval. Arguably, when analyzing real data this latter case is less prejudicial than the former situation as the Eliassen–Palm flux is expected to vanish for quasi-inertial waves (Fritts et al. 2006).

Importantly, since the wave directions of propagation and absolute momentum fluxes are both well retrieved, the zonal and meridional momentum fluxes, respectively $u'w' \equiv u'_{\|}w' \cos\theta$ and $v'w' \equiv u'_{\|}w' \sin\theta$, which are the quantities of interest in GW drag parameterizations, can be estimated from the balloon observations. Typically, the uncertainty in the estimation of the zonal and meridional momentum fluxes is similar to that of the absolute momentum fluxes (~10%) as the wave directions of propagation are almost perfectly retrieved.

The retrieval of the horizontal intrinsic phase speeds is displayed in Fig. 7 for simulations both with and without measurement noise. When the observations are assumed to be perfect, the uncertainty in the retrieved intrinsic phase speeds is relatively small, that is, ~12 m s^{-1} for input phase speeds greater than 20 m s^{-1}. However, the dispersion of the retrieval increases greatly at low intrinsic phase speeds, in which situation a wave is actually perceived as quasi-stationary by the balloon. Therefore, the balloon does not sample adequately the wave packet and the analysis fails. Wave packets with such low intrinsic phase speeds are expected to strongly interact with the mean flow at the level where they are observed and may therefore be of less importance for the forcing of the flow above the balloon float altitude.

When realistic measurement uncertainties are included in the simulations, the retrieval of intrinsic phase speed is significantly degraded. The retrieved phase speeds are overestimated by 60% on average, or by 20% if only waves with $\hat{c} > 20$ m s^{-1} are considered, and the overall 1σ standard deviation of the retrieval is 35 m s^{-1}. There are two main reasons to this deterioration. First, the phase speeds are obtained from the Eulerian component (p'_w) of the wave-induced pressure disturbances, which is generally an order of magnitude smaller than its Lagrangian counterpart and thus typically comparable to the uncertainty in the pressure measurement. Second, the phase shift ϕ between the

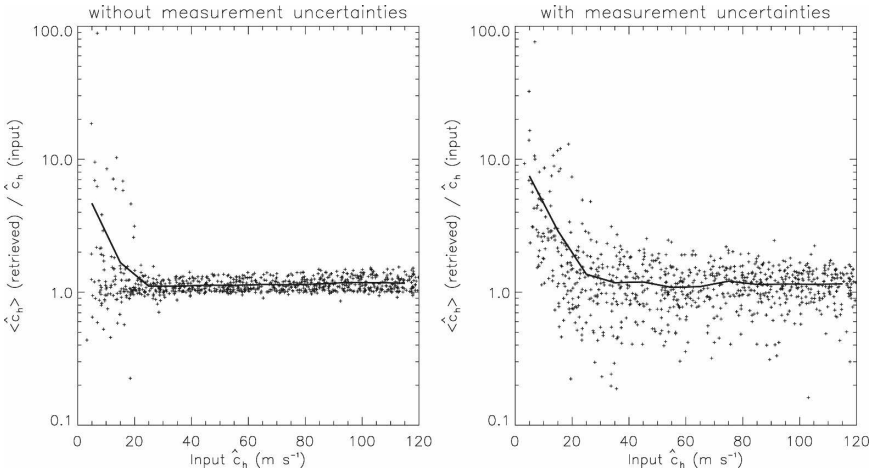

FIG. 7. (left) Ratio of retrieved to input horizontal intrinsic phase speed vs input intrinsic phase speeds obtained with the 1-GW simulations without measurement noise. (right) As in the left panel but for the simulations with measurement noise. The thick line indicates the mean ratio over phase speed intervals of 10 m s^{-1}. Note that a logarithmic scale is used on the y axis.

balloon vertical displacement and that of the isopycnic surface has to be known to compute the wave phase speed using (27). Now, this estimation relies on the density observations, for which the uncertainties are mostly due to the instrumental noise in the temperature measurement. This significantly impacts the accuracy to which ϕ, and consequently $\hat{c}$, can be obtained.

b. *Simulations with multiple gravity wave packets*

In reality, there can be more than one wave packet occurring at any given time. To study how this situation impacts retrievals, we generated two additional sets of 1000 time series with 2 and 10 wave packets in each simulation, respectively. Figure 8 illustrates the wavelet analysis for one simulation in each of the sets. In the two-GW case shown in that figure, both wave packets are still clearly separated by the analysis. When this happens, the retrievals with the two-wave set are very similar to those obtained with the simulations with one wave packet. It was found that they depart significantly only when the wave packets in the two-wave time series occur less than 12 h apart (not shown). In that case, the

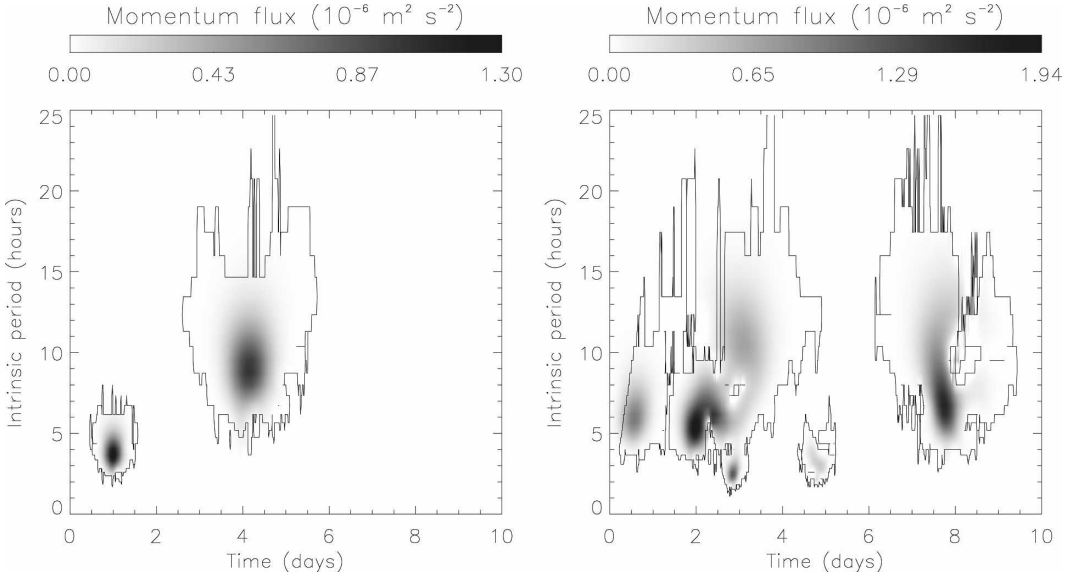

FIG. 8. Momentum flux distribution in time/intrinsic period space in the case of (left) 2 and (right) 10 GW packets in the simulated time series. Wavelet coefficients located inside the solid contour are identified as associated with a wave packet.

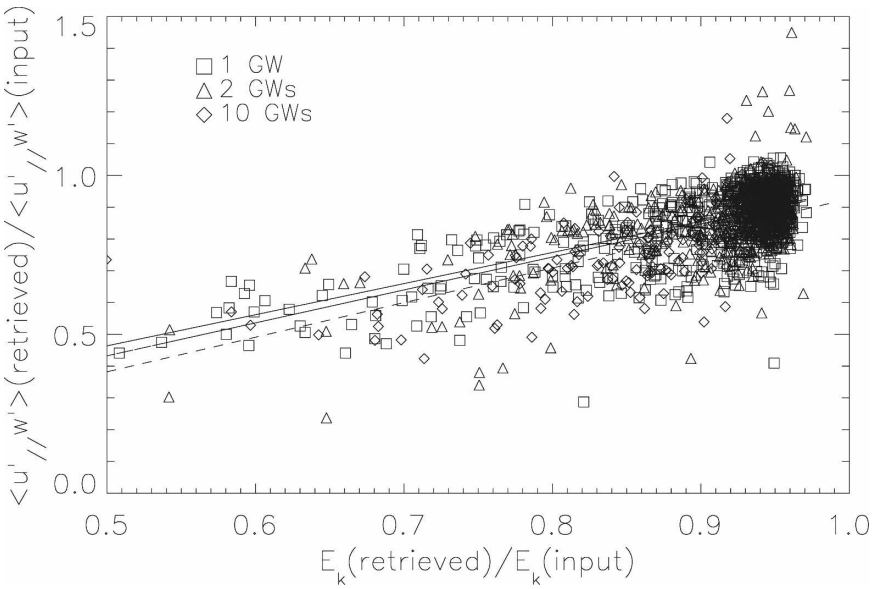

FIG. 9. Ratio of retrieved to input absolute momentum flux vs ratio of retrieved to input horizontal kinetic energy in the simulated time series with 1 (squares), 2 (triangles), and 10 (diamonds) GW packets. From top to bottom, regression lines are shown for the case studies using 1, 2, and 10 wave packets. The retrieved values are computed from the wavelet analysis by summing over the selected wavelet coefficients (see text for further details).

momentum-flux retrieval is slightly noisier and the retrieved momentum flux can, on some occasions, be overestimated.

When 10 wave packets are present, some of the wave packets will always overlap in the time/frequency space, as illustrated in Fig. 8. It is consequently more difficult for the retrieval algorithm to detect the envelope corresponding to each of the various wave packets. This results in a further underestimation of the flight-mean momentum flux. Overall, the momentum-flux underestimation estimated from the simulations is thus 14%, 13%, and 23% in the respective cases with 1, 2, and 10 wave packets in the time series. On the other hand, the 1σ uncertainty in the estimation of the momentum fluxes does not exhibit any significant dependence on the number of wave packets in the time series and varies between 11% and 13%.

It is not possible to use the quoted underestimations to correct results obtained with the real balloon flights since we do not know a priori how many wave packets are present at any given moment in the atmosphere. Nevertheless, we show here that a proxy can be used to determine the amount by which momentum fluxes are underestimated. Namely, the "true" flight-average GW horizontal kinetic energy can be easily estimated in the balloon observations by applying a high-pass filter (with a cutoff frequency corresponding to the smallest inertial frequency during the flight) to the horizontal-velocity time series, so as to isolate the GW signal. On the other hand, a "retrieved" flight-average kinetic energy can be computed from the wavelet analysis as

$$\frac{1}{2}\sum_{t_i}\sum_{j}\{\tilde{u}^2[t_i, \hat{\omega}_j^{\mathrm{gw}}(t_i)] + \tilde{v}^2[t_i, \hat{\omega}_j^{\mathrm{gw}}(t_i)]\}, \qquad (35)$$

where the inner sum extends once again over the wavelet coefficients selected as corresponding to GW packets found at the ith observation record. The proxy is then simply computed as the ratio of the retrieved kinetic energy [obtained from (35)] to the true kinetic energy (estimated with the filtered time series). Figure 9 displays the correlation between the momentum-flux underestimation and the kinetic-energy proxy. Whatever the number of wave packets in the simulated time series, the regression lines are very similar, indicating that this kinetic-energy proxy can be used to estimate by how much our algorithm underestimates GW momentum fluxes.

c. Directions of propagation and phase speeds

In contrast with the case with one wave packet in the simulated time series, (34) cannot be used to estimate either the retrieved phase speeds or the retrieved directions of propagation when several wave packets are present. Instead, Fig. 10 compares the input and retrieved distributions of the flight-mean density-

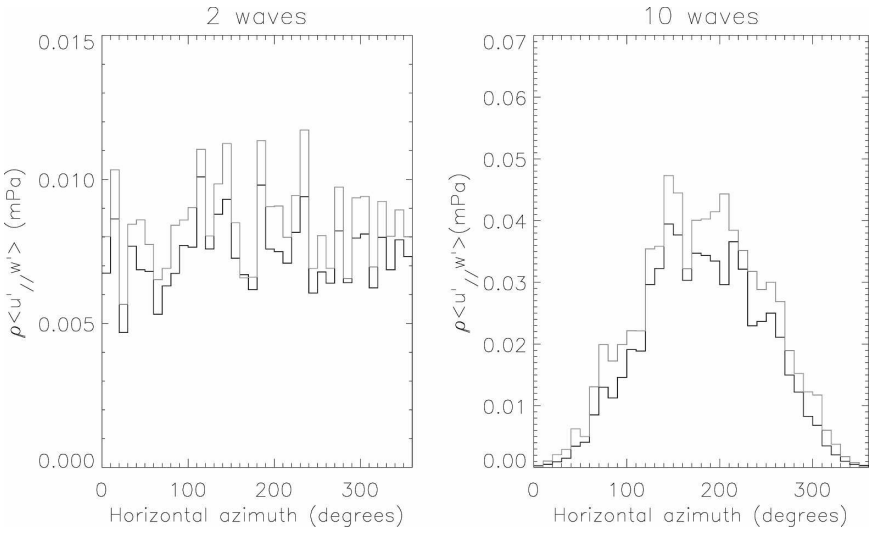

FIG. 10. (left) Distribution of flight-mean density-weighted absolute momentum fluxes $\rho\overline{u'_{//}w'}$ as a function of wave direction of propagation in the 1000 simulations with two wave packets: input distribution (gray) and retrieved distribution (black). (right) As in the left panel but for simulations with 10 wave packets. Note that the vertical scale differs between the two graphs.

weighted absolute momentum fluxes $\rho\overline{u'_{//}w'}$ as a function of the directions of propagation. The result is the average over all simulations of the $\rho\overline{u'_{//}w'}(\theta)$ distributions.

In the simulations with two GW packets (Fig. 10, left panel), the input absolute momentum fluxes are independent of the wave directions of propagation, as highlighted by the input distribution. There is a clear correlation between the input and retrieved distributions, which indicates that the directions of propagation are still correctly estimated by the algorithm when only two wave packets are present. It is also noticeable that the retrieved momentum fluxes are slightly smaller than the input values.

In the simulations with ten GW packets on the other hand, a distinct dependence of momentum flux on the direction of propagation was deliberately imposed (Fig. 10, right panel); namely, the momentum fluxes scale as $\sin^2(\theta/2)$ (i.e., there are larger westward than eastward fluxes). This nonisotropic distribution allows us to test the reliability of the retrieval by comparing input and retrieved propagation directions. The good agreement observed in the right panel of Fig. 10 demonstrates that wave propagation directions are, indeed, reliably retrieved, even in the case of a large number of wave packets.

The distributions of density-weighted zonal momentum fluxes $\rho\overline{u'w'}$ as a function of the zonal phase speeds $\hat{c}_x$ are displayed in Fig. 11. As for the directions of propagation, this figure displays the average over all the simulations of the $\rho\overline{u'w'}(\hat{c}_x)$ distributions. In our simulations, the momentum fluxes depend on the intrinsic phase speeds through a $\hat{\omega}^{-1}$ scaling so that the input distributions have more momentum flux at low phase speeds. In the case of the two-wave packet simulations, the retrieved distribution is approximately the same as the input. However, the phase speed retrieval is less accurate at low phase speeds, in agreement with the results obtained with the single-wave simulations. A significant part of the momentum flux is also wrongly attributed to high phase speed waves so that the overall retrieved distribution is somewhat broader than the input distribution. These defects are amplified when 10 wave packets are present in the simulations. In that case, an even more significant amount of momentum flux is attributed to phase speeds larger than the largest phase speed used in the simulations. Nevertheless, the strong anisotropy of the input distribution is correctly reproduced by the retrieval algorithm.

5. Summary

A methodology is presented to extract information on GW characteristics from the meteorological observations gathered during long-duration, superpressure balloon flights in the stratosphere. This methodology is based on wavelet analysis techniques that enables GW packets to be identified in the observational time series. When applied to real time series, the wavelet analysis is very useful for studying the geographical distribution of GW activity.

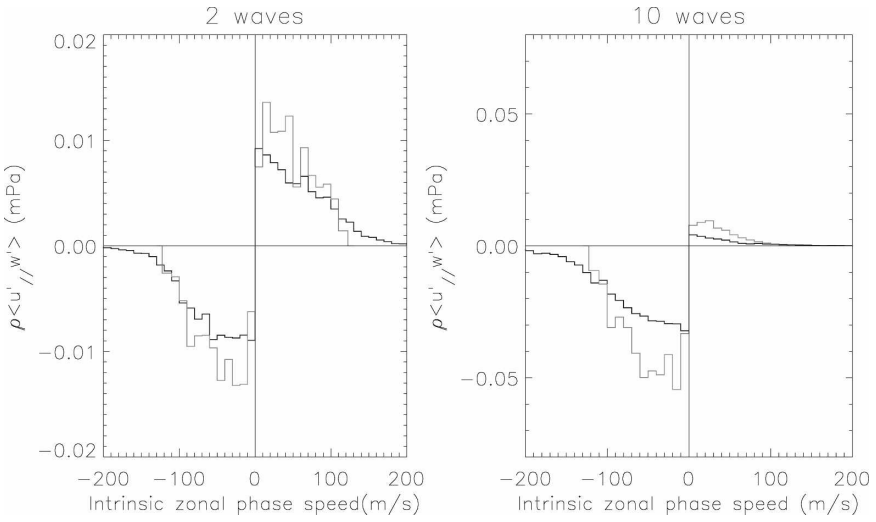

FIG. 11. (left) Distribution of flight-mean density-weighted zonal momentum fluxes $\rho\overline{u'w'}$ as a function of intrinsic zonal phase speeds $\hat{c}_x$ for the simulations with two wave packets: input distribution (gray) and retrieved distribution (black). (right) As in the left panel but for the simulations with 10 wave packets. Note that the vertical scale differs between the two plots.

Correlations between the velocity and Lagrangian pressure disturbances are used to infer GW momentum fluxes and phase speeds. The method was applied to simulated balloon observations containing up to 10 distinct wave packets. The prescribed wave distributions are generally well retrieved from the simulated observations. Absolute momentum fluxes are well estimated, despite a slight low bias. The underestimation is particularly evident for the highest frequency waves that we can resolve (intrinsic periods of 1–2 h) and is due to the 15-min sampling used during the Vorcore campaign. A proxy aimed at quantifying the overall underestimation can, nevertheless, be easily computed from the balloon observations and can be used to correct the estimated momentum fluxes a posteriori. Since the wave propagation directions are almost perfectly retrieved by our method, the zonal and meridional momentum fluxes are typically estimated with the same accuracy as the absolute momentum fluxes.

On the other hand, GW phase speeds are retrieved much less accurately than the momentum fluxes or directions of propagation. In particular, waves with low intrinsic phase speeds are inadequately sampled by the balloons, which induces a significant dispersion in the retrieval. In general, our method tends to overestimate the phase speeds.

The methodology described in this article is applied in Hertzog et al. (2008) to the dataset gathered during the Stratéole/Vorcore campaign and enables us to study GW activity above Antarctica and in the Southern Hemisphere midlatitudes.

Acknowledgments. AH, FV, and GB acknowledge support of long-duration balloon activities from CNES and CNRS/INSU. RAV acknowledges travel support from the Scientific Visits to Europe Scheme of the Australian Academy of Science and Department of Science and Environment, and the visiting program from École Polytechnique. The authors would also like to thank the two anonymous reviewers who contributed to significantly improve the manuscript.

REFERENCES

Alexander, M. J., and L. Pfister, 1995: Gravity wave momentum flux in the stratosphere over convection. *Geophys. Res. Lett.,* **22,** 2029–2032.

——, and C. Barnet, 2007: Using satellite observations to constrain parameterizations of gravity wave effects for global models. *J. Atmos. Sci.,* **64,** 1652–1665.

——, and Coauthors, 2008: Global estimates of gravity wave momentum flux from High Resolution Dynamics Limb Sounder observations. *J. Geophys. Res.,* **113,** D15S18, doi:10.1029/2007JD008807.

Allen, S. J., and R. A. Vincent, 1995: Gravity wave activity in the lower atmosphere: Seasonal and latitudinal variations. *J. Geophys. Res.,* **100,** 1327–1350.

Andrews, D. G., J. R. Holton, and C. B. Leovy, 1987: *Middle Atmosphere Dynamics.* Academic Press, 490 pp.

Baumgaertner, A. J. G., and A. J. McDonald, 2007: A gravity wave climatology for Antarctica compiled from Challenging Minisatellite Payload/Global Positioning System (CHAMP/GPS) radio occultations. *J. Geophys. Res.,* **112,** D05103, doi:10.1029/2006JD007504.

Charron, M., E. Manzini, and C. D. Warner, 2002: Intercomparison of gravity wave parameterizations: Hines Doppler-spread

and Warner and McIntyre ultra-simple schemes. *J. Meteor. Soc. Japan,* **80,** 335–345.

Eckermann, S. D., and P. Preusse, 1999: Global measurements of stratospheric mountain waves from space. *Science,* **286,** 1534–1537.

——, and D. L. Wu, 2006: Imaging gravity waves in the lower stratospheric AMSU-A radiances. Part 1: Simple forward model. *Atmos. Chem. Phys.,* **6,** 3325–3341.

Ern, M., P. Preusse, M. J. Alexander, and C. D. Warner, 2004: Absolute values of gravity wave momentum flux derived from satellite data. *J. Geophys. Res.,* **109,** D20103, doi:10.1029/2004JD004752.

——, ——, and C. D. Warner, 2006: Some experimental constraints for spectral parameters in the Warner and McIntyre gravity wave parameterization scheme. *Atmos. Chem. Phys.,* **6,** 4361–4381.

Fetzer, E. J., and J. C. Gille, 1994: Gravity wave variance in LIMS temperatures. Part I: Variability and comparison with background winds. *J. Atmos. Sci.,* **51,** 2461–2483.

Fritts, D. C., and G. D. Nastrom, 1992: Sources of mesoscale variability of gravity waves. Part II: Frontal, convective, and jet stream excitation. *J. Atmos. Sci.,* **49,** 111–127.

——, and M. J. Alexander, 2003: Gravity wave dynamics and effects in the middle atmosphere. *Rev. Geophys.,* **41,** 1003, doi:10.1029/2001RG000106.

——, T. Tsuda, T. E. VanZandt, S. A. Smith, T. Sato, S. Fukao, and S. Kato, 1990: Studies of velocity fluctuations in the lower atmosphere using the MU radar. Part II: Momentum fluxes and energy densities. *J. Atmos. Sci.,* **47,** 51–66.

——, S. L. Vadas, K. Wan, and J. A. Werne, 2006: Mean and variable forcing of the middle atmosphere by gravity waves. *J. Atmos. Solar Terr. Phys.,* **68,** 247–265.

Hertzog, A., and F. Vial, 2001: A study of the dynamics of the equatorial lower stratosphere by use of ultra-long-duration balloons. 2. Gravity waves. *J. Geophys. Res.,* **106,** 22 745–22 761.

——, ——, C. R. Mechoso, C. Basdevant, and P. Cocquerez, 2002: Quasi-Lagrangian measurements in the lower stratosphere reveal an energy peak associated with near-inertial waves. *Geophys. Res. Lett.,* **29,** 1229, doi:10.1029/2001GL014083.

——, and Coauthors, 2007: Stratéole-Vorcore—Long-duration, superpressure balloons to study the Antarctic lower stratosphere during the 2005 winter. *J. Atmos. Oceanic Technol.,* **24,** 2048–2061.

——, G. Boccara, R. A. Vincent, F. Vial, and P. Cocquerez, 2008: Estimation of gravity wave momentum flux and phase speeds from quasi-Lagrangian stratospheric balloon flights. Part II: Results from the Vorcore campaign in Antarctica. *J. Atmos. Sci.,* **65,** 3056–3070.

Holton, J. R., P. H. Haynes, M. E. McIntyre, A. R. Douglass, R. B. Hood, and L. Pfister, 1995: Stratosphere–troposphere exchange. *Rev. Geophys.,* **33,** 405–439.

Jiang, J. H., S. D. Eckermann, D. L. Wu, and J. Ma, 2004: A search for mountain waves in MLS stratospheric limb radiances from the winter Northern Hemisphere: Data analysis and global mountain wave modeling. *J. Geophys. Res.,* **109,** D03107, doi:10.1029/2003JD003974.

Massman, W. J., 1978: On the nature of vertical oscillations of constant volume balloons. *J. Appl. Meteor.,* **17,** 1351–1356.

——, 1981: An investigation of gravity waves on a global scale using TWERLE data. *J. Geophys. Res.,* **86,** 4072–4082.

McLandress, C., and J. F. Scinocca, 2005: The GCM response to current parameterizations of nonorographic gravity wave drag. *J. Atmos. Sci.,* **62,** 2394–2413.

——, M. J. Alexander, and D. L. Wu, 2000: Microwave Limb Sounder observations of gravity waves in the stratosphere: A climatology and interpretation. *J. Geophys. Res.,* **105,** 11 947–11 967.

Nastrom, G. D., 1980: The response of superpressure balloons to gravity waves. *J. Appl. Meteor.,* **19,** 1013–1019.

——, and D. C. Fritts, 1992: Sources of mesoscale variability of gravity waves. Part I: Topographic excitation. *J. Atmos. Sci.,* **49,** 101–110.

Preusse, P., A. Dörnbrack, S. D. Eckermann, M. Riese, B. Schaeler, J. T. Bacmeister, D. Broutman, and K. U. Grossmann, 2002: Space-based measurements of stratospheric mountain waves by CRISTA. 1. Sensitivity, analysis method, and a case study. *J. Geophys. Res.,* **107,** 8178, doi:10.1029/2001JD000699.

Ratnam, M. V., G. Tetzlaff, and C. Jacobi, 2004: Global and seasonal variations of stratospheric gravity wave activity deduced from the *CHAMP*/GPS satellite. *J. Atmos. Sci.,* **61,** 1610–1620.

Steiner, A. K., and G. Kirchengast, 2000: Gravity wave spectra from GPS/MET occultation observations. *J. Atmos. Oceanic Technol.,* **17,** 495–503.

Torrence, C., and G. P. Compo, 1998: A practical guide to wavelet analysis. *Bull. Amer. Meteor. Soc.,* **79,** 61–78.

Tsuda, T., Y. Murayama, M. Yamamoto, S. Kato, and S. Fukao, 1990: Seasonal variation of momentum flux in the mesosphere observed with the MU radar. *Geophys. Res. Lett.,* **17,** 725–728.

——, M. Nishida, C. Rocken, and R. H. Ware, 2000: A global morphology of gravity wave activity in the stratosphere revealed by GPS occultation data (GPS/MET). *J. Geophys. Res.,* **105,** 7257–7273.

Vincent, R. A., and I. M. Reid, 1983: HF Doppler measurements of mesospheric gravity wave momentum fluxes. *J. Atmos. Sci.,* **40,** 1321–1333.

——, A. Hertzog, G. Boccara, and F. Vial, 2007: Quasi-Lagrangian superpressure balloon measurements of gravity-wave momentum fluxes in the polar stratosphere of both hemispheres. *Geophys. Res. Lett.,* **34,** L19804, doi:10.1029/2007GL031072.

Wu, D. L., 2004: Mesoscale gravity wave variances from AMSU-A radiances. *Geophys. Res. Lett.,* **31,** L12114, doi:10.1029/2004GL019562.

——, and J. W. Waters, 1996: Gravity-wave-scale temperature fluctuations seen by UARS MLS. *Geophys. Res. Lett.,* **23,** 3289–3292.